Pressure-induced switching between topological phases in magnetic van der Waals heterostructures

Jie Li [1,*] Peiru Yang,[1] Wei Ren,[2] and Ruqian Wu [3,†]

[1]*School of Materials Science and Engineering, Shanghai University, Shanghai 200444, China*

[2]*International Centre for Quantum and Molecular Structures and Department of Physics, Shanghai University, Shanghai 200444, China*

[3]*Department of Physics and Astronomy, University of California, Irvine, California 92697-4575, USA*

(Received 15 September 2023; accepted 18 December 2023; published 17 January 2024)

Despite the significant developments in quantum anomalous Hall (QAH) insulators study in recent years, it remains an outstanding challenge to tune between different topological phases in the same material. In this work, an ultrathin van der Waals (vdW) heterostructure based on $MnBi_2Se_4$ and Bi_2Se_3 was proposed by using model Hamiltonian and density-functional theory simulations, which was proved to be an excellent tunable QAH platform. Its band gap closes and reopens as hydrostatic pressure increases, with a topological phase transition around the critical pressure of 2.5 GPa. Further analyses reveal the main reason is the enhancement of interlayer interactions and the crystal-field splitting as the interlayer distance decreases. Our work provides clear physical insights and suggests a strategy for experimental realization and control of the QAH effect in real materials.

DOI: 10.1103/PhysRevB.109.035419

I. INTRODUCTION

The quantum anomalous Hall (QAH) effect has garnered significant research attention owing to its profound importance in fundamental science as well as its potential applications in various nanotechnologies such as spintronics and quantum information [1–3]. Despite the remarkable progress made in recent years, the design and tuning of QAH insulators, especially the integration of multiple topological phases in a single material, still remain as outstanding challenges [4–6]. In a scheme of quantum phase transition between the QAH insulator and normal insulator states, "on" corresponds to the ballistic flow of charge and spin dissipationlessly along edges of a QAH insulator, and "off" is produced by applying an appropriate stimulus that converts the material to a normal insulator with no conductive channels. This controllability is promising for the exploitation in nanosensors, low-energy logic circuits, and quantum information devices [7–9]. The quest for novel functional materials and effective tuning methods emerges as a crucial and urgent multidisciplinary research endeavor for advancing technological development of QAH-based devices.

Due to the unique layered structure and the relatively weak van der Waals (vdW) interlayer interaction, vdW heterostructures constructed by stacking different 2D materials have been actively explored as new powerful platforms for attaining exotic physical phenomena, from low-dimensional ferromagnetism [10], unconventional topological phase [11], ferroelectricity or multiferroicity [12,13], photovoltaics [14], and superconductivity [15]. Recently, extensive studies established that mechanical engineering of crystal lattices such as hydrostatic pressure can reversibly modulate the electronic and magnetic properties of various materials [16–18]. For vdW heterostructures, in particular, hydrostatic pressure can drastically reduce the interlayer separations, and hence enhance the interlayer vdW interaction and modulate the band structure. This approach may induce diverse phase transitions [15,18–20], and presents a strategy to effectively control material properties in a conventional manner. Conversely, it also enables the detection of pressure change due to significantly reduced modulus of vdW materials compared to most semiconductors.

In this work, we explore the possibility of tuning magnetic vdW heterostructures between normal and QAH insulator phases (N-Q) with a hydrostatic pressure. Using a low-energy effective Hamiltonian model, we demonstrate that the N-Q topological phase transition can be induced by either increasing the exchange field or decreasing the mutual interaction between two surface states. Accordingly, we propose a vdW heterostructure with one Bi_2Se_3 (BS) quintuple layer sandwiched by a homology $MnBi_2Se_4$ (MBS) septuple layer in each side (MBS/BS/MBS) as a model system and explore the possibility of using hydrostatic or tensile pressure to control its properties. Density-functional theory (DFT) calculations indicate the effectiveness of tuning the topological properties of the MBS/BS/MBS heterostructure with pressure. These findings suggest not only a strategy but also a practical material platform for the experimental realization of the switching of the QAH effect, which is imperative for the development of topological materials and devices.

II. METHODOLOGY

For all the density-functional theory calculations in this work, we choose the Vienna *Ab initio* Simulation Package (VASP) at the level of the spin-polarized generalized-gradient approximation with the functional developed by Perdew, Burke, and Ernzerhof [21]. The framework of the projector

*lij@shu.edu.cn
†wur@uci.edu

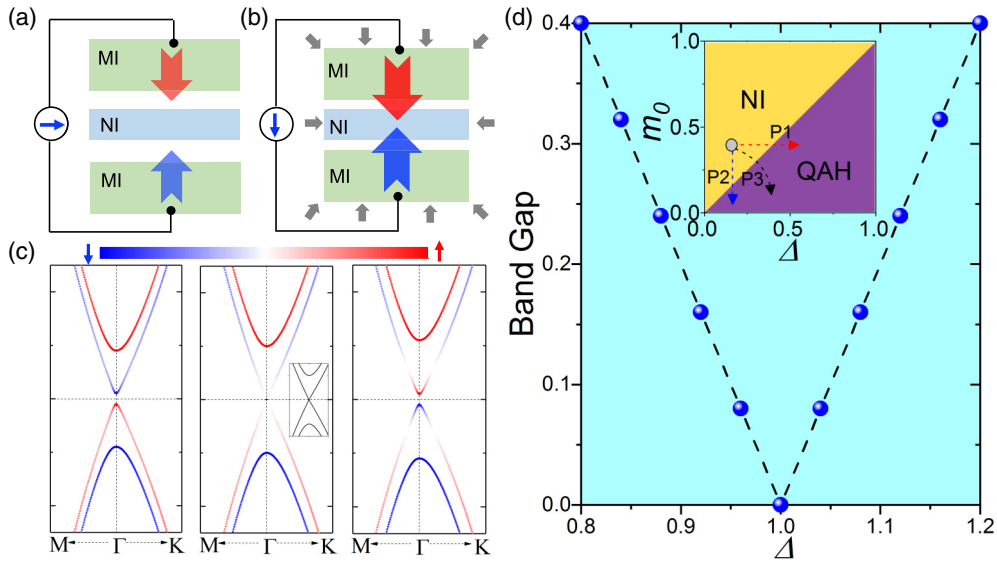

FIG. 1. Schematic diagram of a thin vdW heterostructure without (a) and with pressures (b); red and blue arrows represent the exchange field and gray arrows represent the hydrostatic pressure. (c) Evolution of band structures with the increasing exchange field (Δ). (d) The band gap as a function of Δ from model calculations (the inset is phase diagram from model calculations; the boundary separates the normal insulator and QAH phases).

augmented-wave method was adopted to treat the interaction between valence electrons and ionic cores [22,23]. For the electron correlation in the *d* shells of Mn cores, we adopt the Hubbard *U* of 4.0 eV [24]. The vdW correction (DFT-D3) was included to well describe the dispersion forces [25]. In all DFT calculations, the energy cutoff for the plane-wave basis expansion is set to 500 eV, and the criterion for total energy convergence is set at 10^{-5}eV. For the atomic relaxation under hydrostatic pressure, a bulk cell with MBS/BS/MBS thin films sandwiched between two half-period MBSs was built, and all atoms were fully relaxed using the conjugated gradient method for the energy minimization until the force on each atom became smaller than 0.01 eV/Å. The one-dimensional (1D) band of nanoribbon is calculated with a tight-binding (TB) model based on the maximally localized Wannier functions, as implemented in the WANNIER90 code [26].

III. RESULTS AND DISCUSSION

A. Low-energy effective Hamiltonian model prediction

As shown in Fig. 1(a), we design a simple symmetric model, featuring a slab of a normal insulator (NI) with a small band gap and the capability to transition into a topological phase. This slab is sandwiched by two ferromagnetic insulator (MI) layers so the surface states near the Fermi level are magnetized. Such geometries have been synthesized in experiments by stacking various layered vdW materials and have the capability to integrate multiple functionalities. The potential emergent quantum states from the hybridization of two interfaces between NI layer and MI overlayers can be analyzed by using a low-energy effective Hamiltonian model [2,27]. Based on a basis set of $|t\uparrow\rangle$, $|t\downarrow\rangle$, $|b\uparrow\rangle$, and $|b\downarrow\rangle$, with t and b representing the top and bottom surface states and $\uparrow,\downarrow$ representing the spin-up and spin-down states, the low-energy effective Hamiltonian is [4,27]

$$H(k) = H_{sf}(k) + H_{\text{Zeeman}}(k) + H_{if}(k) = \begin{bmatrix} 0 & iv_f k_- & m(k) & 0 \\ -iv_f k_+ & 0 & 0 & m(k) \\ m(k) & 0 & 0 & -iv_f k_- \\ 0 & m(k) & iv_f k_+ & 0 \end{bmatrix} + \begin{bmatrix} \Delta & 0 & 0 & 0 \\ 0 & -\Delta & 0 & 0 \\ 0 & 0 & \Delta & 0 \\ 0 & 0 & 0 & -\Delta \end{bmatrix} + \begin{bmatrix} V & 0 & 0 & 0 \\ 0 & V & 0 & 0 \\ 0 & 0 & -V & 0 \\ 0 & 0 & 0 & -V \end{bmatrix},$$

where H_{sf}, H_{Zeeman}, and H_{if} represent the surface states, the exchange field (with strength Δ) caused by the proximity effect of the MI, and the potential difference (with strength V) between the two interfaces, respectively. $k_\pm = k_x \pm ik_y$, v_f is the Fermi velocity, and $m(k) = m_0 + m_1(k_x^2 + k_y^2)$ describes the interaction between the top and bottom surface states. From the analysis for $V = 0$, we find that the magnetic vdW heterostructure has one phase boundary ($\Delta = m_0$) as shown in the inset of Fig. 1(d), i.e., the left region ($\Delta < m_0$) is for NI and the right region ($\Delta > m_0$) corresponds to the QAH

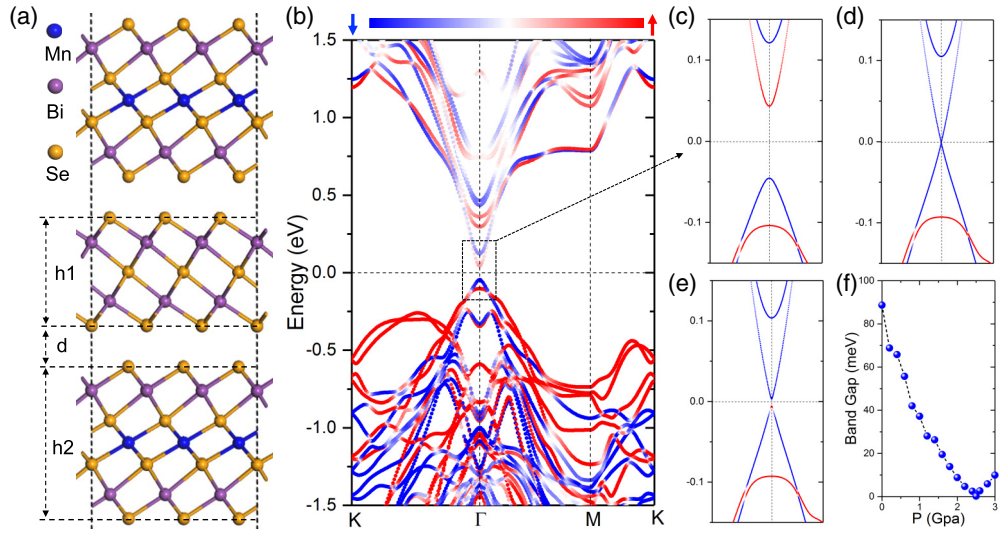

FIG. 2. (a) Atomic structure of MBS/BS/MBS. (b) The band structure of MBS/BS/MBS. (c)–(e) The zoom-in band structures of MBS/BS/MBS near the Fermi level around the Γ point with hydrostatic pressure (P) of 0.00, 2.5, and 3.0 GPa, respectively. (f) The band gap as a function of hydrostatic pressure.

phase, respectively. A magnetic vdW heterostructure in the left region, possibly with large m_0, is a candidate for the N-Q topological phase transition. Typically, m_0 of a vdW heterostructure can be adjusted by controlling the film thickness, i.e., m_0 increases as the film thickness decreases. From the phase diagram, one may see that there are three paths for the N-Q topological phase transition, namely, increasing the exchange field (P1), decreasing the mutual interaction between two surface states (P2), or a combination of both (P3). With the evolution of bands of magnetic vdW heterostructures along P1 (P2) paths in Fig. 1(c) and Fig. S1 (in the Supplemental Material [28]), the topologically trivial band gap can be narrowed to closed and reopened as Δ (m_0) increases (decreases), accompanied by a band inversion.

B. DFT verifications: Structural and electronical properties

Based on the model analysis conducted, it is determined that vdW heterostructures exhibiting the N-Q topological phase transition should have the following characteristics: a relatively small thickness ($m_0 > \Delta$), a large spin-orbit coupling (SOC), a flat interface, and accessibility for synthesis. In this work, we propose a design of an ultrathin vdW heterostructure by sandwiching a quintuple layer of Bi_2Se_3 between two septuple layers of $MnBi_2Se_4$ (MBS/BS/MBS) as illustrated in Fig. 2(a). As the lattice mismatch between MBS and BS is negligible (4.10 vs 4.14 Å) [29,30], we keep the lattice size of MBS/BS/MBS at 4.14 Å for the convenience of calculations. Test calculations indicate that electronic properties of MBS are not much affected by this slight expansion. Following the structural optimization process, which includes the vdW correction in the calculations, the resulting interlayer distance between MBS and BS is 2.69 Å. The binding energy, defined as $E_b = E_{BS} + 2E_{MBS} - E_{vdW}$, is 0.69 eV per supercell in MBS/BS/MBS, indicating a weak but stable interlayer binding in this vdW heterostructure. Here, E_{BS}, E_{MBS}, and E_{vdW} are the total energies of BS, MBS, and MBS/BS/MBS slabs, respectively. To further check its dynamic stability, *ab initio* molecular dynamics (AIMD) simulations is performed at 300 K for 10 ps, using a 5 × 5 supercell with 475 atoms. The simulation results indicate that no noticeable structural deformation occurs throughout the entire simulation period. Additionally, the total energy of the system fluctuates around the equilibrium value without sudden jump (see Fig. S2 in the Supplemental Material [28]). Based on these observations, it can be inferred that the MBS/BS/MBS heterostructure is thermally stable up to at least room temperature. Considering that BS and MBS are homology materials and many similar sandwich vdW heterostructures have already been grown with molecular-beam epitaxy [29,31,32], it is reasonable to assume that there are no significant technological barriers to synthesizing MBS/BS/MBS.

To investigate whether MBS/BS/MBS may exhibit the predicted N-Q topological phase transition, we conduct DFT calculations and examine its electronic band structure according to the expectations set by the low-energy effective Hamiltonian model. As shown in Fig. 2(b), Dirac-type surface states with a band gap of 88.7 meV can be found across the Fermi level, which is a desirable feature for the N-Q topological phase transition. By fitting the DFT bands near the Γ point, we may extract parameters Δ and m_0 for the low-energy effective Hamiltonian model. The obtained values are $\Delta = 0.034$ eV and $m_0 = 0.078$ eV, respectively. These results indicate that MBS/BS/MBS meets the criterion of $m_0 > \Delta$ for the N-Q topological phase transition according to the model prediction. DFT calculations show that this system has large negative Berry curvature near the Γ point, and positive Berry curvature in the peripheral regions as in Figs. 3(a) and 3(b). As the integration of Berry curvature in the Brillouin zone equals zero, this band gap is topologically trivial.

Now, we search for appropriate approach to tune Δ or m_0 for the N-Q topological phase transition. Inspired by the success of pressure-controlled magnetism [18–20], we first apply hydrostatic pressure (P) as the control method. The P-induced

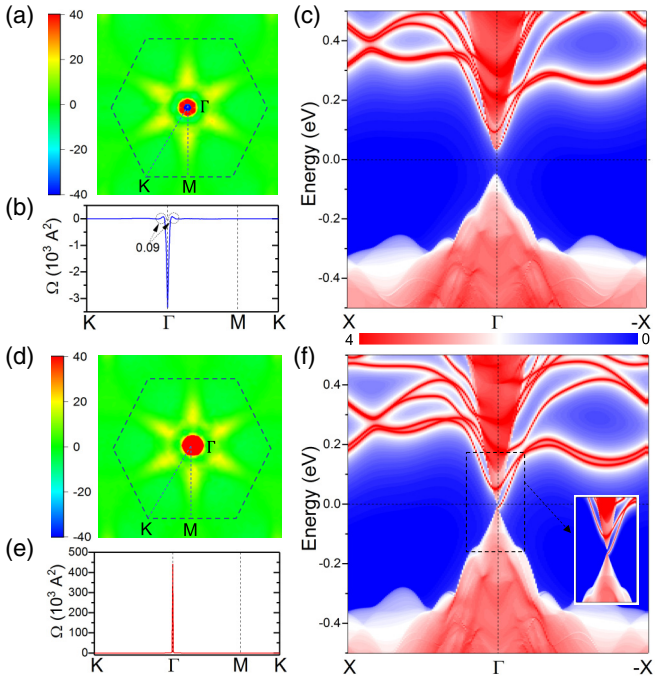

FIG. 3. (a), (b) The distribution of Berry curvature in the 2D Brillouin zone and along high-symmetry path for MBS/BS/MBS without hydrostatic pressure, respectively, (c) The corresponding 1D band structure. (d), (f) The corresponding situations for MBS/BS/MBS with hydrostatic pressure of 3.0 GPa.

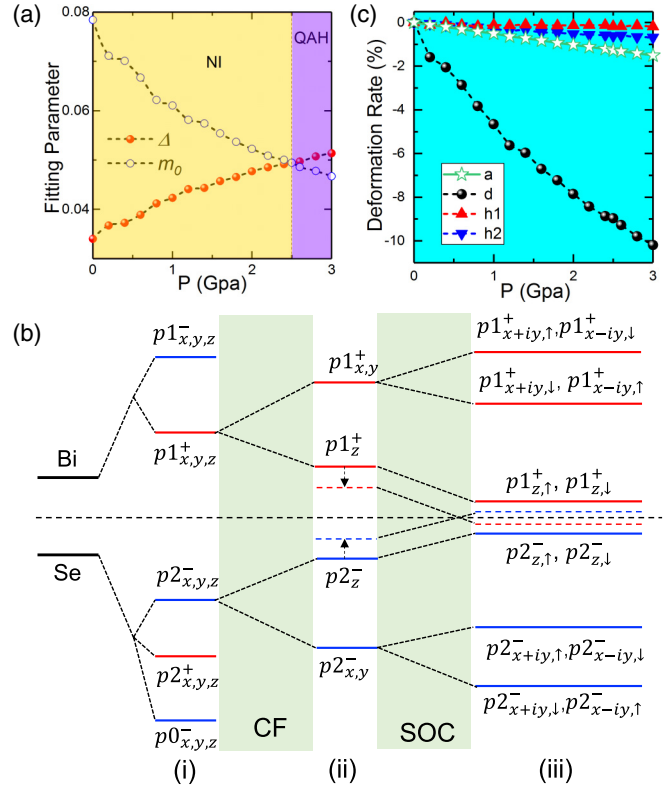

FIG. 4. (a) The fitting parameters Δ and m_0 extracted from the band structures of MBS/BS/MBS under hydrostatic pressure. (b) Schematic diagram of the evolution of atomic energy levels on the energy eigenvalues at the Γ point with the effect of crystal-field splitting and SOC included; three different stages (i), (ii), and (iii) represent the effect of turning on chemical bonding, crystal-field splitting, and SOC, respectively (the black dashed line represents the Fermi energy). (c) The deformation rate of the in-plane lattice constant, interlayer distance, and thickness of BS and MBS of MBS/BS/MBS under hydrostatic pressure.

change in bands of MBS/BS/MBS is schematically shown in Figs. 2(c)–2(f). The band gap gradually decreases with P, then increases with the watershed at ∼2.5 GPa. Importantly, a clear band inversion between the spin-up and spin-down bands can be seen at the Γ point before and after the gap closure (see Fig. 2), which aligns well with the model prediction as depicted in Fig. 1(c). To verify the occurrence of the N-Q topological phase transition, the Berry curvature $\Omega(k)$ of MBS/BS/MBS with P of 3.0 GPa is calculated in the Brillouin zone as shown in Fig. 3(d). Compared to the counterparts without hydrostatic pressure, a different situation can be seen; in particular, the large negative Berry curvature near the Γ point now turns to be positive. As a result, the integration of Berry curvature over the Brillouin zone gives a nonzero Chern number $C = 1$, and the Hall conductance has a quantized value, $\sigma_{xy} = C(e^2/\hbar)$. In other word, MBS/BS/MBS becomes a QAH insulator with a P of 3.0 GPa.

To further verify the N-Q topological phase transition, we perform calculations for MBS/BS/MBS nanoribbons with the TB approach using parameters extracted from the DFT bands. Without the hydrostatic pressure, there is no edge state in the bulk gap [see Fig. 3(c)]. In contrast, one edge state is present in the bulk gap for the case with a hydrostatic pressure of 3.0 GPa [see Fig. 3(f)]. Obviously, the N-Q topological phase transition can be produced and controlled by a hydrostatic pressure on the MBS/BS/MBS heterostructure.

C. N-Q topological phase transition mechanism

To get a clear picture of the N-Q topological phase transition, fitting parameters Δ and m_0 are extracted from the band structures of MBS/BS/MBS under different values of P. As shown in Fig. 4(a), Δ (m_0) increases (decreases) with P, respectively, and Δ crosses m_0 at $P = 2.5$ GPa. The P-induced N-Q topological phase transition is hence along the P3 path as depicted in the inset of Fig. 1(d). The energy eigenvalues at the Γ point and projections to atomic orbitals are adopted to schematically illustrate the band inversion. With the interplay of crystal-field splitting and SOC, there are three stages of orbital crossing as shown in Fig. 4(b). From the spatial distributions of surface states near the Γ point and the projected density of states (PDOS) of MBS/BS/MBS (see Figs. S4 and S5 in the Supplemental Material [28]), one may see that the surface states near the Fermi level mainly result from p orbitals of Bi and Se atoms, especially in the interfacial region. We thus may neglect the s orbitals and reconstruct the surface-state wave function with p orbitals of Bi and Se atoms as shown in stage (i) in Fig. 4(b). There are two states (one odd, one even) from p orbitals of Bi atoms and three states (two odd, one even) from p orbitals of Se atoms, which are labeled as $|p1^{\pm}_{x,y,z}\rangle$, $|p2^{\pm}_{x,y,z}\rangle$, and $|p0^{-}_{x,y,z}\rangle$, with $+$, $-$ standing for the parity of the states [33]. When crystal-field splitting is included, p orbitals split to p_z

and twofold degenerate $p_{x/y}$ in the C_{3v} symmetry. $|p1^+_{,z}\rangle$ and $|p2^-_{,z}\rangle$ are on two sides of the Fermi level as shown in stage (ii) (supported by the plots of PDOS of MBS/BS/MBS in Fig. S5 in the- Supplemental Material [28]). In stage (iii), the SOC mixes spin and orbital angular momenta, and induces a level repulsion between $|p1^+_{,z}\uparrow\rangle$ and $|p1^+_{,x+iy}\downarrow\rangle$ as well as between $|p1^+_{,z}\downarrow\rangle$ and $|p1^+_{,x-iy}\uparrow\rangle$. Similar situations also occur for $|p2^-_{,z}\uparrow,\downarrow\rangle$ and $|p2^-_{,x\pm iy}\downarrow,\uparrow\rangle$, which leads to downshifts (upshifts) of the $|p1^+_{,z}\uparrow,\downarrow\rangle$ and $(|p2^-_{,z}\uparrow,\downarrow\rangle)$ states, and the band gap thus decreases. If SOC is sufficiently strong, a level inversion and consequently topological phase transition occur. For the free MBS/BS/MBS, the band gap is larger than SOC, so a hydrostatic pressure is needed to produce the topological state by enhancing the crystal-field splitting [18,34] which consequently leads to a decrease of band gap without SOC, as schematically shown by the dashed lines in Fig. 4(b). This is also suggested from the changes of band structures of MBS/BS/MBS before and after hydrostatic pressure (see Fig. S6 in the Supplemental Material [28]). The inclusion of SOC introduces a notable level inversion in the system, as can be observed in the spatial distribution of surface states near the Γ point of the MBS/BS/MBS structure under a hydrostatic pressure of 3.0 GPa. This phenomenon is detailed in Fig. S9 of the Supplemental Material [28]. Such a level inversion is a critical factor that triggers the N-Q topological phase transition, and highlights the intricate interplay between SOC, external pressure, and the electronic properties of the material.

Obviously, hydrostatic pressure-induced N-Q phase transition stems from the lattice geometry change. We define the deformation rates (D) of the in-plane lattice constant (a), interlayer distance (d), and thickness of BS and MBS layers ($h1$, $h2$) by

$$D = (x_p - x_0)/x_0 \times 100\%,$$

where x_0 and x_p represent a, d, $h1$, and $h2$ of MBS/BS/MBS before and after hydrostatic pressure, respectively. From the DFT calculations [see Fig. 4(c)], one can see that these lattice constants decrease continuously as hydrostatic pressure increases, and the interlayer distance is much more sensitive to hydrostatic pressure than the in-plane lattice constant and thickness, due to the weaker interlayer vdW interactions compared to the intralayer covalent interactions. Obviously, a significant compressional anisotropy is present in MBS/BS/MBS, which is similar to what was experimentally observed in $MnBi_2Te_4$ [20]. High hydrostatic pressure causes the decrease of interlayer distance and the enhancement of magnetizations of Bi and Se atoms, especially in the interface regions (see the spin density in Fig. S7 in the Supplemental Material [28]). The magnetocrystalline anisotropy (MCA) of MBS/BS/MBS is also enhanced from 112 μeV per supercell to 202 μeV per supercell with hydrostatic pressure increasing to 3.0 GPa. DFT calculations show that the increase of MCA under pressure mainly results from the contribution of the Bi atoms near to the interface (see the magnetocrystalline anisotropy in Fig. S8 in the Supplemental Material [28]). Obviously, the decrease of interlayer distance under hydrostatic pressure strengthens the proximity effect and crystal-field splitting of the p orbitals (partially seen in the spatial distributions of surface states near the Γ point in Fig. S9 in the Supplemental Material [28]). Therefore, the large deformation in d should be the main reason for the hydrostatic pressure-induced N-Q topological phase transition for MBS/BS/MBS. In fact, DFT calculations show very similar results if we freeze the in-plane lattice constant and apply tensile stress (see Fig. S10 in the Supplemental Material [28]). In addition, DFT calculations show that MBS/BS/MBS has smaller modulus (see Table S1 in the Supplemental Material [28]) than other materials such as $\alpha - Al_2O_3$, Si, and graphite [35–37].

IV. CONCLUSION

In summary, by using model simulations and DFT calculations, we found that MBS/BS/MBS vdW heterostructure is an excellent candidate for the control of the QAH state via hydrostatic pressure. Although the MBS/BS/MBS vdW heterostructure we proposed has a trivial gap of 88.7 meV in ambient condition, this gap can be closed and reopened to a topologically nontrivial gap as hydrostatic pressure is applied. This pressure-induced N-Q topological phase transition can be used for sensing and spintronic applications. Furtherly analysis shows that the hydrostatic pressure induces large decrease of interlayer distance in MBS/BS/MBS, which leads to the enhanced interactions across the BS and MBS interface. For this reason, tensile stress was found to produce very similar results. Although the critical pressure for the N-Q transition in MBS/BS/MBS appears to be high, the possibility of making quantum phase transition with pressure in vdW heterostructures may inspire broad interest in searching for practical combinations for the easy control of the QAH effect. Indeed, the richness and flexibility of vdW heterostructures provide a wide range of platforms for harnessing the QAH effect, paving the way for technological innovations.

ACKNOWLEDGMENTS

This work was partially supported by the startup foundation from Shanghai University and the National Natural Science Foundation of China (Grant No. 12304089). Calculations were partially performed on computers at Shanghai Technical Service Center of Science and Engineering Computing, Shanghai University. R.W. acknowledges support by U.S. DOE, Basic Energy Science (Grant No. DE-FG02-05ER46237 and computing allocation at National Energy Research Scientific Computing Center).

[1] C. Z. Chang, J. Zhang, X. Feng, J. Shen, Z. Zhang, M. I. Guo, K. Li, Y. Ou, P. Wei, L. L. Wang, Z. Q. Ji, Y. Feng, S. Ji, X. Chen, J. Jia, X. Dai, Z. Fang, S. C. Zhang, K. He, Y. Wang, L. Lu, X. C. Ma, and Q. K. Xue, Experimental observation of the quantum anomalous Hall effect in a magnetic topological insulator, Science **340**, 167 (2013).

[2] W. Zhang, R. Yu, H. J. Zhang, S. C. Zhang, X. Dai, and Z. Fang, Quantized anomalous Hall effect in magnetic topological insulators, Science **329**, 61 (2010).

[3] Y. J. Deng, Y. J. Yu, M. Z. Shi, Z. X. Guo, Z. Xu, J. Wang, X. H. Chen, and Y. B. Zhang, Quantum anomalous Hall effect in intrinsic magnetic topological insulator $MnBi_2Te_4$, Science **367**, 895 (2020).

[4] A. Gaikwad, S. Sun, P. Wang, L. Zhang, J. Gano, X. Dai, and X. Du, Strain-tuned topological phase transition and unconventional Zeeman effect in $ZrTe_5$ microcrystals, Commun. Mater. **3**, 94 (2022).

[5] Z. Qiao, W. Ren, H. Chen, L. Bellaiche, Z. Zhang, A. H. MacDonald, and Q. Niu, Quantum anomalous Hall effect in graphene proximity coupled to an antiferromagnetic insulator, Phys. Rev. Lett. **112**, 116404 (2014).

[6] C. Chen, J. Zeng, Y. Ren, L. Fang, Y. Wu, P. Zhang, T. Hu, J. Wang, Z. Qiao, and W. Ren, In-plane magnetization and electronic structures in $BiFeO_3$/graphene superlattice, Appl. Phys. Lett. **120**, 084002 (2022).

[7] W. G. Vandenberghe and M. V. Fischetti, Imperfect two-dimensional topological insulator field-effect transistors, Nat. Commun. **8**, 14184 (2017).

[8] J. L. Collins, A. Tadich, W. Wu, L. C. Gomes, J. N. B. Rodrigues, C. Liu, J. Hellerstedt, H. Ryu, S. Tang, S. K. Mo, S. Adam, S. A. Yang, M. S. Fuhrer, and M. T. Edmonds, Electric-field-tuned topological phase transition in ultrathin Na_3Bi, Nature (London) **564**, 390 (2018).

[9] C. Lin, M. Ochi, R. Noguchi, K. Kuroda, M. Sakoda, A. Nomura, M. Tsubota, P. Zhang, C. Bareille, K. Kurokawa, Y. Arai, K. Kawaguchi, H. Tanaka, K. Yaji, A. Harasawa, M. Hashimoto, D. Lu, S. Shin, R. Arita, S. Tanda, and T. Kondo, Visualization of the strain-induced topological phase transition in a quasi-one-dimensional superconductor $TaSe_3$, Nat. Mater. **20**, 1093 (2021).

[10] Y. Li, B. Yang, S. Xu, B. Huang, and W. Duan, Emergent phenomena in magnetic two-dimensional materials and van der Waals heterostructures, ACS Appl. Electron. Mater. **4**, 3278 (2022).

[11] B. Huang, M. A. McGuire, A. F. May, D. Xiao, P. Jarillo-Herrero, and X. Xu, Emergent phenomena and proximity effects in two-dimensional magnets and heterostructures, Nat. Mater. **19**, 1276 (2020).

[12] X. Wang, C. Zhu, Y. Deng, R. Duan, J. Chen, Q. Zeng, J. Zhou, Q. Fu, L. You, S. Liu, J. H. Edgar, P. Yu, and Z. Liu, Van der Waals engineering of ferroelectric heterostructures for long-retention memory, Nat. Commun. **12**, 1109 (2021).

[13] C. Gong, E. M. Kim, Y. Wang, G. Lee, and X. Zhang, Multiferroicity in atomic van der Waals heterostructures, Nat. Commun. **10**, 2657 (2019).

[14] K. K. Paul, J. H. Kim, and Y. H. Lee, Hot carrier photovoltaics in van der Waals heterostructures, Nat. Rev. Phys. **3**, 178 (2021).

[15] W. Li, J. Feng, X. Zhang, C. Li, H. Dong, W. Deng, J. Liu, H. Tian, J. Chen, S. Jiang, H. Sheng, B. Chen, and H. Zhang, Metallization and superconductivity in the van der Waals compound CuP_2Se through pressure-tuning of the interlayer coupling, J. Am. Chem. Soc. **143**, 20343 (2021).

[16] Y. Liu, Y. Y. Li, S. Rajput, D. Gilks, L. Lari, P. L. Galindo, M. Weinert, V. K. Lazarov, and L. Li, Tuning Dirac states by strain in the topological insulator Bi_2Se_3, Nat. Phys. **10**, 294 (2014).

[17] C. Lei, S. Chen, and A. H. MacDonald, Magnetized topological insulator multilayers, Proc. Natl Acad. Sci. USA **117**, 27224 (2020).

[18] Z. Xu, M. Ye, J. Li, W. Duan, and Y. Xu, Hydrostatic pressure-induced magnetic and topological phase transitions in the $MnBi_2Te_4$ family of materials, Phys. Rev. B **105**, 085129 (2022).

[19] T. Li, S. Jiang, N. Sivadas, Z. Wang, Y. Xu, D. Weber, J. E. Goldberger, K. Watanabe, T. Taniguchi, C. J. Fennie, K. F. Mak, and J. Shan, Pressure-controlled interlayer magnetism in atomically thin CrI_3, Nat. Mater. **18**, 1303 (2019).

[20] K. Y. Chen, B. S. Wang, J. Q. Yan, D. S. Parker, J. S. Zhou, Y. Uwatoko, and J. G. Cheng, Suppression of the antiferromagnetic metallic state in the pressurized $MnBi_2Te_4$ single crystal, Phys. Rev. Mater. **3**, 094201 (2019).

[21] J. P. Perdew, K. Burke, and M. Ernzerhof, Generalized gradient approximation made simple, Phys. Rev. Lett. **77**, 3865 (1996).

[22] P. E. Blöchl, Projector augmented-wave method, Phys. Rev. B **50**, 17953 (1994).

[23] G. Kresse and D. Joubert, From ultrasoft pseudopotentials to the projector augmented-wave method, Phys. Rev. B **59**, 1758 (1999).

[24] S. L. Dudarev, G. A. Botton, S. Y. Savrasov, C. J. Humphreys, and A. P. Sutton, Electron-energy-loss spectra and the structural stability of nickel oxide: An LSDA+ U study, Phys. Rev. B **57**, 1505 (1998).

[25] S. Grimme, J. Antony, S. Ehrlich, and S. Krieg, A consistent and accurate *ab initio* parametrization of density functional dispersion correction (DFT-D) for the 94 elements H-Pu, J. Chem. Phys. **132**, 154104 (2010).

[26] A. A. Mostofi, J. R. Yates, G. Pizzi, Y. S. Lee, I. Souza, D. Vanderbilt, and N. Marzari, An updated version of wannier90: A tool for obtaining maximally-localised Wannier functions, Comput. Phys. Commun. **185**, 2309 (2014).

[27] J. Wang, B. Lian, and S. C. Zhang, Electrically tunable magnetism in magnetic topological insulators, Phys. Rev. Lett. **115**, 036805 (2015).

[28] See Supplemental Material at http://link.aps.org/supplemental/10.1103/PhysRevB.109.035419 for the details of other results from effective Hamiltonian model calculations, AIMD simulations of MBS/BS/MBS, the fitting band structures by using the wannier90 package, the spatial distributions of surface states, the band structures, spin density, and magnetocrystalline anisotropy of MBS/BS/MBS under hydrostatic pressure of 0.0 and 3.0 GPa, the charge density of surface states near the Γ point of MBS/BS/MBS, band structure of MBS/BS/MBS with tensile stress, and elastic constants of MBS/BS/MBS.

[29] T. Zhu, A. J. Bishop, T. Zhou, M. Zhu, D. J. O'Hara, A. A. Baker, S. Cheng, R. C. Walko, J. J. Repicky, T. Liu, J. A. Gupta, C. M. Jozwiak, E. Rotenberg, J. Hwang, I. Žutić, and R. K. Kawakami, Synthesis, magnetic properties, and electronic structure of magnetic topological insulator $MnBi_2Se_4$, Nano Lett. **21**, 5083 (2021).

[30] T. Hirahara, S. V. Eremeev, T. Shirasawa, Y. Okuyama, T. Kubo, R. Nakanishi, R. Akiyama, A. Takayama, T. Hajiri, S. Ideta, M. Matsunami, K. Sumida, K. Miyamoto, Y. Takagi, K. Tanaka, T. Okuda, T. Yokoyama, S. Kimura, S. Hasegawa, and E. V. Chulkov, Large-gap magnetic topological heterostructure formed by subsurface incorporation of a ferromagnetic layer, Nano Lett. **17**, 3493 (2017).

[31] J. Shao, Y. Liu, M. Zeng, J. Li, X. Wu, X. M. Ma, F. Jin, R. Lu, Y. Sun, M. Gu, K. Wang, W. Wu, L. Wu, C. Liu, Q. Liu, and Y. Zhao, Pressure-tuned intralayer exchange in superlattice-like $MnBi_2Te_4/(Bi_2Te_3)_n$ topological insulators, Nano Lett. **21**, 5874 (2021).

[32] Q. Li, C. X. Trang, W. Wu, J. Hwang, D. Cortie, N. Medhekar, S. K. Mo, S. A. Yang, and M. T. Edmonds, Large magnetic gap in a designer ferromagnet-topological insulator-ferromagnet heterostructure, Adv. Mater. **34**, 2107520 (2022).

[33] H. Zhang, C. X. Liu, X. L. Qi, X. Dai, Z. Fang, and S. C. Zhang, Topological insulators in Bi_2Se_3, Bi_2Te_3 and Sb_2Te_3 with a single Dirac cone on the surface, Nat. Phys. **5**, 438 (2009).

[34] P. L. Gong, D. Y. Liu, K. S. Yang, Z. J. Xiang, X. H. Chen, Z. Zeng, S. Q. Shen, and L. J. Zou, Hydrostatic pressure induced three-dimensional Dirac semimetal in black phosphorus, Phys. Rev. B **93**, 195434 (2016).

[35] S. Shang, Y. Wang, and Z. K. Liu, First-principles elastic constants of α- and θ-Al_2O_3, Appl. Phys. Lett. **90**, 101909 (2007).

[36] O. Beckstein, J. E. Klepeis, G. L. W. Hart, and O. Pankratov, First-principles elastic constants and electronic structure of a-Pt_2Si and PtSi, Phys. Rev. B **63**, 134112 (2001).

[37] K. H. Michel and B. Verberck, Theory of the elastic constants of graphite and graphene, Phys. Status Solidi B **245**, 2177 (2008).